

# Improvements in the Maximum THz Output Power and Responsivity in Near-Ballistic Uni-Traveling-Carrier Photodiodes With an Undercut Collector

Yu-Cyuan Huang, Nan-Wei Chen , Yen-Kun Wu, Naseem , and Jin-Wei Shi , *Senior Member, IEEE*

**Abstract**—We demonstrate a novel ultra-fast photodiode structure that fundamentally relaxes the trade-offs between the speed, responsivity, and saturation power at sub-THz regime. Our device, with its 3  $\mu\text{m}$  wide undercut collector profile, exhibits a DC responsivity (0.11 A/W) which is close in value to that reported for uni-traveling-carrier photodiodes (UTC-PDs) with similar sized active diameters ( $\sim 10 \mu\text{m}$ ), but has a much larger 3-dB optical-to-electrical (O-E) bandwidth (220 GHz vs. around 75 GHz). This leads to much less optical power being required to deliver a close value of THz output power at the same operating frequency. Furthermore, the responsivity (0.11 vs. 0.1 A/W) and output power (0.4 vs.  $-2.4 \text{ dBm}@165 \text{ GHz}$ ) are higher than those of reference devices without the undercut collector layer but with a miniaturized active diameter as small as 3  $\mu\text{m}$ .

**Index Terms**—Photodiode, ultrafast optics.

## I. INTRODUCTION

APPLYING photonic technology to the next-generation (6G) millimeter-wave (MMW) wireless communication system is desirable in order to achieve a quantum jump in the transmission data rate; this could be done with the adoption of a carrier frequency as high as  $> 95 \text{ GHz}$  in future 6G systems [1]. However, the MMW carrier signal suffers a much higher propagation loss in free space than the radio-frequency (RF) carrier waves used in modern wireless communication systems. One possible solution to increase the coverage of a wireless network would require the installation of large numbers of pico- or femto-cells in the 6G system [2], although the management of numerous femtocells during system operation would be challenging. Fortunately, the radio-over-fiber (RoF) technology

provides a way to effectively coordinate such cells. In an RoF access fronthaul network, optical MMW (local oscillator; LO) and data signals can be generated in the central office and then transmitted to antennas in numerous cell site cabins through low-loss optical fibers. Since each cell shares the same optical LO signal, smart beam forming and steering becomes feasible through central office control [2], [3]. In such a scenario, the ultrafast and high-power photodiodes (PDs) in each cell would play an important role in converting the incoming optical LO signal into an MMW signal, determining the maximum available bandwidth and dynamic range [4], [5], [6], [7] of the whole system.

The limitations caused by the trade-off between speed and output power encountered in the traditional p-i-n PDs have been successfully overcome by modifying the structure of uni-traveling carrier photodiodes (UTC-PDs) [8], [9], [10], which have only an electron as an active carrier [11], [12], [13], [14], [15].

Downscaling the thickness of the depletion layer and the size of the device active area are essential to minimizing both the internal carrier transient time and the RC-limited bandwidth in order to boost the speed of the PD to near the THz regime [8], [9], [10], [11], [12], [13], [14], [15], [16]. It is usually necessary for the UTC-PD to have an active diameter of less than 10  $\mu\text{m}$  [12], [14], [15] for a bandwidth of around 100 GHz, but this leads to significant optical coupling loss, limited alignment tolerance during PD packaging, and a degradation in the dc responsivity performance. The edge-coupled structure of the waveguide-integrated PD (WGPD) has been demonstrated to effectively release the trade-off between the bandwidth and responsivity in ultrafast PDs with a miniaturized size [8]. The WGPDs have demonstrated excellent performance in the THz regime [16]. Nevertheless, as is also the case for vertically-illuminated PDs, the difficulties with optical coupling and alignment tolerance both remain challenges for ultra-fast WGPDs.

The combination of a substrate lens with the flip-chip bonding package has become an effective solution to overcome the above-mentioned problems in ultra-fast PDs. This approach has been applied to improve the commercially available miniaturized PDs and packaged PD modules, to achieve an excellent bandwidth of over 50 GHz, large alignment tolerance, and a high dc

Manuscript received 18 August 2023; revised 29 October 2023, 29 November 2023, and 1 December 2023; accepted 5 December 2023. Date of publication 7 December 2023; date of current version 2 April 2024. This work was supported by the National Science and Technology Council in Taiwan under Grant 109-2221-E-008-081-MY3. (Corresponding author: Jin-Wei Shi.)

Yu-Cyuan Huang, Yen-Kun Wu, Naseem, and Jin-Wei Shi are with the Department of Electrical Engineering, National Central University, Taoyuan 320, Taiwan (e-mail: allanychuang@gmail.com; wsx980260905@gmail.com; naseemever3@gmail.com; jwshi@ee.ncu.edu.tw).

Nan-Wei Chen is with the Department of Electrical Engineering, Yuan Ze University, Taoyuan 320, Taiwan (e-mail: nwchen@saturn.yzu.edu.tw).

Color versions of one or more figures in this article are available at <https://doi.org/10.1109/JLT.2023.3340502>.

Digital Object Identifier 10.1109/JLT.2023.3340502

responsivity of 0.8 A/W [17]. However, the unavoidable parasitic capacitance induced by flip-chip bonding packaging results in a degradation in bandwidth for the packaged PD module [18], [19].

In this work, we demonstrate a novel UTC-PD structure with an undercut collector profile capable of overcoming the trade-offs between the speed, saturation power, and device active area. This is similar in concept to that realized for the traditional  $\text{In}_{0.53}\text{Ga}_{0.47}\text{As}/\text{InP}$  p-i-n photodiode, in which the undercut profile in the intrinsic  $\text{In}_{0.53}\text{Ga}_{0.47}\text{As}$  absorption layer further enhances the speed performance [8], [20].

This novel UTC-PD structure, which has a  $11\ \mu\text{m}$  active diameter and a  $3\ \mu\text{m}$  collector width, in combination with an optimized flip-chip bonding package, demonstrates a higher responsivity (0.11 vs. 0.1 A/W), higher saturation current (9 vs. 7 mA), and larger output power (0.4 vs.  $-2.4\ \text{dBm}@165\text{GHz}$ ) than those of the reference devices with miniaturized active diameters ( $3\ \mu\text{m}$ ). Although our undercut device has a smaller net O-E bandwidth (220 vs. 280 GHz) than that of the reference one due to its larger parasitic capacitance, it still has a superior bandwidth performance to that of the reported ultra-fast UTC-PDs ( $\sim 75$  [14] vs. 220 GHz) with similar sized active diameters ( $\sim 10\ \mu\text{m}$ ) [12], [14] and a similar responsivity performance (0.11 A/W), thanks to this novel undercut collector design. The demonstrated ultrafast PD structure with flip-chip bonding package fundamentally relaxes the trade-offs between the speed, responsivity, and saturation power of UTC-PD at sub-THz regime

## II. DESIGN AND FABRICATION OF THE DEVICE STRUCTURE

Fig. 1(a) and (b), respectively, show a conceptual cross-sectional view and the simulated band diagram of our demonstrated device structure. The epi-layer structure was grown on a semi-insulating (S.I.) InP substrate in a molecular-beam epitaxy (MBE) chamber<sup>1</sup>. As can be seen, the absorption region is comprised of a p-type  $\text{InGa}_{0.53}\text{As}_{0.47}$  absorption layer with a thickness of 160 nm and a graded doping profile (top:  $1 \times 10^{19}\ \text{cm}^{-3}$  to bottom:  $1 \times 10^{17}\ \text{cm}^{-3}$ ) designed to accelerate the electron diffusion process.

A thin (20 nm) n-type graded bandgap layer, with a  $\text{In}_x\text{Al}_y\text{Ga}_{1-x-y}\text{As}$  ( $x: 0.52; y: 0.04$  to  $0.25$ ) structure, was inserted between the intrinsic i)  $-\text{In}_{0.53}\text{Ga}_{0.47}\text{As}$  and 20 nm InP field control layer with light p-type doping ( $3 \times 10^{16}\ \text{cm}^{-3}$ ). The inclusion of an extra p-n junction inside the collector layer effectively controls the drop of the electron potential in the absorption-collector junction, suppresses the current blocking effect [10], [14], and allows the electron overshoot drift-velocity to be sustained even under a higher reverse bias voltage [11]. When the operation frequency of the UTC-PD is near the THz regime ( $> 200\ \text{GHz}$ ), the optimum bias for maximizing the speed and THz output power usually happens at a small reverse bias voltage (less than  $-1\ \text{V}$ ) [10]. Such a small bias voltage is usually accompanied by a pronounced external circuit saturation effect, which can be minimized by reducing the load resistance of the PD at the expense of a lower output THz power. In our previous work, we successfully demonstrated a near-ballistic UTC-PD

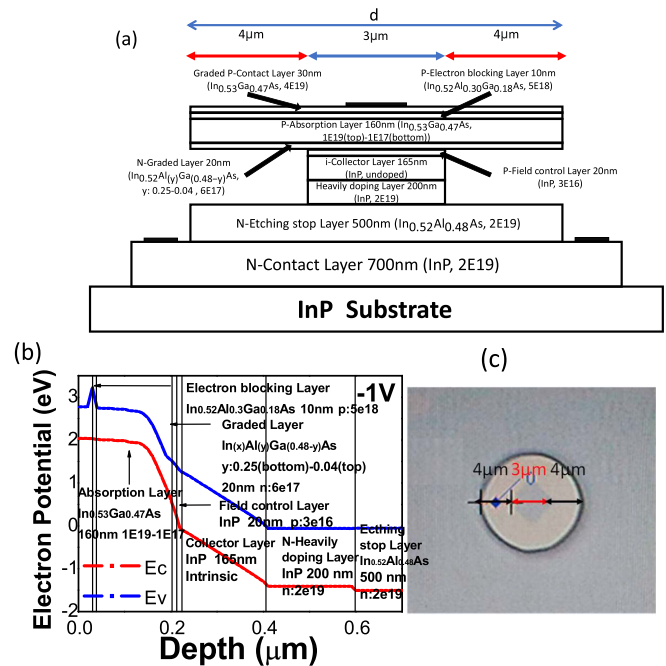


Fig. 1. (a) Conceptual cross-sectional view of the device where “d” represents the total width of the absorption layers. (b) Simulated band diagram of the demonstrated NBUTC-PDs under a bias voltage of  $-1\ \text{V}$ . The unit for doping density in each layer is  $\text{cm}^{-3}$ . (c) Top-view of active mesa of device C with the undercut collector profile.

(NBUTC-PD) structure with an extra p-type field control layer within the collector that could increase the optimum bias voltage and further increase the output power under a  $50\ \Omega$  load [11], [21]. In addition, there was an extra 500 nm thick n+  $\text{In}_{0.52}\text{Al}_{0.48}\text{As}$  etching stop layer buried below the InP collector layer for the undercut etching process, as shown in Fig. 1(b). The whole collector layer and the extra p-n junction for field control can be fully depleted under a moderate reverse bias voltage of  $-1\ \text{V}$ . For this current work, PDs with three different active diameters of 3, 9, and  $11\ \mu\text{m}$  (devices A to C) were fabricated. The major difference between the PD fabrication process reported in our previous work [10] and the one applied in this study was the adoption of an additional undercut wet etching process for the fabrication of devices B and C. The same dry etching process was used to define the active mesas of these 3 devices (A to C), which had 3 different diameters, as noted above. Then, devices B and C were immersed in a mixed chemical solution ( $\text{HCl}:\text{H}_3\text{PO}_4:\text{CH}_3\text{COOH} = 1:1:2$ ) for the formation of an undercut profile in the InP collector layer. The width of the undercutting in the collector layer was controlled by properly controlling the wet etching time (through reference to the test key). It was set to be the same in both devices,  $3\ \mu\text{m}$ , as shown in Fig. 1(a). During the process, although the etching rate was faster at the periphery of the device than that at the center, there was still around 70% of the workable device located around the center of the whole chip. Fig. 1(c) shows a top-view picture of device C after the wet etching process. The suspended  $\text{In}_{0.53}\text{Ga}_{0.47}\text{As}$  absorption layer ( $\sim 160\ \text{nm}$ ) is so thin that it is nearly transparent under visible light illumination. The width of

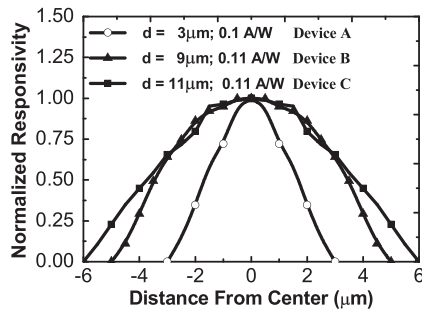


Fig. 2. Normalized DC responsivities of devices A, B and C measured at different distances from the center of the active mesa. Here, “d” stands for the total width of the absorption layers.

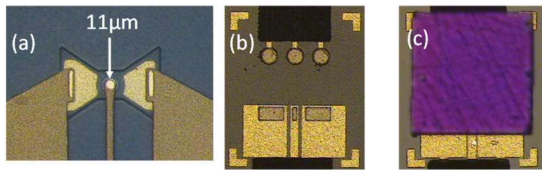


Fig. 3. Top-view of the (a) the active PD chip, (b) bonding pads on the AlN substrate, and (c) PD chip after flip-chip bonding.

the undercut profile layer can thus be measured using an optical microscope. The diamond shape of the undercut mesa arises from the anisotropic wet etching process, which may cause a current crowding effect at the corners of the undercut mesa and some degradation in the high-power performance.

After the mesa etching and metallization processes, the device was directly passivated by the application of spin-on coating of polyimide (PI) film. Since the PI was in a liquid state during this process, it could penetrate the slits in the undercut profile and fully cover the whole of the active mesa. Finally, an anti-reflective (AR) coating was deposited on the back side of the chip. The measured DC responsivity of devices B and C was around 0.11 A/W. Another large device with an active diameter as wide as that of device C (11  $\mu\text{m}$ ) was also fabricated but without performing the undercut process. This was done to minimize the optical coupling loss and investigate the intrinsic responsivity performance of our device design. This device has a measured DC responsivity of up to 0.127 A/W, but due to its large junction capacitance, the O-E bandwidth ( $\sim 60$  GHz) was far below the THz frequency so is excluded from the discussion in the following sections.

When the active diameter of the device was downscaled to 3  $\mu\text{m}$  (device A), there was a degradation in the responsivity, to 0.10 A/W, due to the coupling and diffraction loss between the optical beam and the active mesa. Fig. 2 shows the normalized DC responsivity measured at different lateral distances from the center of the active mesa. It can be clearly seen that the undercut mesa structure not only allows a higher responsivity (0.11 vs. 0.1 A/W) but also a 90% larger alignment tolerance ( $\pm 1.5$  vs.  $\pm 0.5$   $\mu\text{m}$ ).

Fig. 3(a) to (c) show a top-view of the active PD chip, the co-planar waveguide (CPW) pad on the AlN substrate in the flip-chip bonding package, and the PD chip after flip-chip

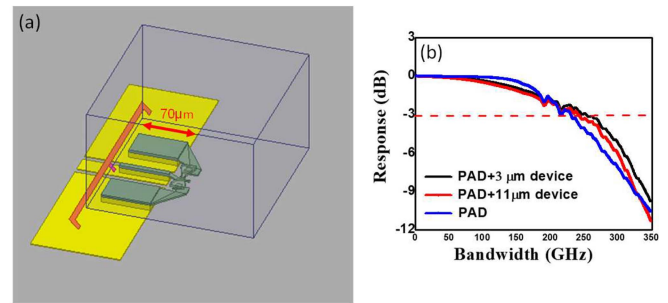


Fig. 4. (a) 3-D structure of the PDs with the flip-chip bonding package used for full-wave analysis and (b) the simulated O-E frequency responses of our 3-D structure with and without (devices A and C) the inclusion of active PD (pad).

bonding packaging. The CPW layout on both sides of the active PD and the AlN carrier has a decisive influence on the net O-E bandwidth of the packaged PD module. Since high-frequency simulations of active p-n junctions with our simulation tool<sup>1</sup> were such a challenge, here, an extracted equivalent-circuit model of the active PD [18], [19] was inserted into the 3-D structure of the flip-chip bonding package for full-wave analysis, which will be discussed in more detail later; see Fig. 9. From the simulation results we can find the optimal layouts for the CPW pads on the semi-insulating InP substrate and AlN carrier needed to maximize the O-E bandwidth [18], [19]. Fig. 4(a) shows the 3-D structure of the device with the flip-chip bonding package used for the full-wave analysis<sup>1</sup>. Fig. 4(b) shows the simulated O-E frequency responses of the packaged module without insertion of the active PD model (pad) and with the circuit models of devices A and C, respectively. The internal frequency response of the carrier transit time, which is far above the measured 3-dB O-E bandwidth (540 vs. 280 GHz) is neglected in the simulation. As can be seen, device A achieved a nearly 0.3 THz 3-dB bandwidth after packaging. The quoted bandwidth numbers are close to our measurement and modeling results, as will be discussed in greater detail later.

### III. MEASUREMENT RESULTS

A heterodyne beating system was used to measure the dynamic performance of the fabricated device structure. A power meter with a sensor head which covers the frequency range from dc to 50 GHz, was used for measurement. When the measurement frequency was greater than 75 GHz, a thermal MMW power meter (PM4, VDI-Erickson), which could cover the 75 GHz to THz measurement frequency regime, was used. The maximum measurement bandwidth for our system was limited by the WR-3.4 waveguide based MMW probe, which operated at around 325 GHz<sup>2</sup>.

From dc to 50 GHz, the frequency dependent loss arising from the passive components mainly originates from the radio-frequency (RF) probe, coaxial cable, and bias tee; it is typically around 6 dB at 50 GHz operation. The value of the frequency dependent loss was carefully verified using a broadband network

<sup>1</sup>ANSYS HFSS: 3D full-wave electromagnetic field simulator, ANSYS, Inc.

<sup>2</sup>GGB Industries, Inc., P.O. BOX 10958, NAPLES, FL 34101.

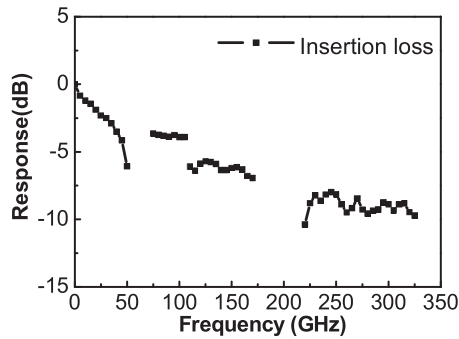


Fig. 5. The frequency response of insertion loss in our hetero-dyne beating measurement system.

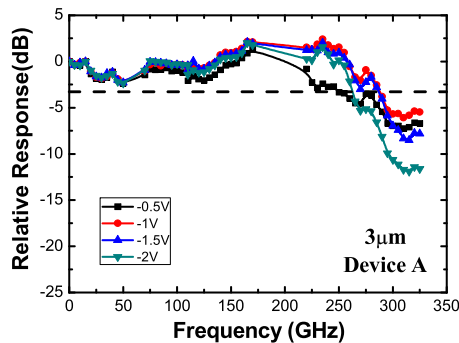


Fig. 6. Bias dependent O-E frequency responses measured under a fixed output photocurrent as 5 mA for device A with an active diameter of 3  $\mu\text{m}$ .

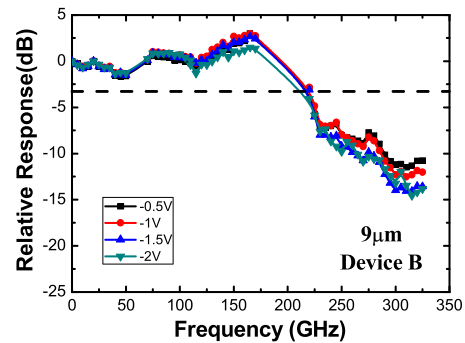


Fig. 7. Bias dependent O-E frequency responses measured under a fixed output photocurrent as 5 mA for device B with an active diameter of 9  $\mu\text{m}$ .

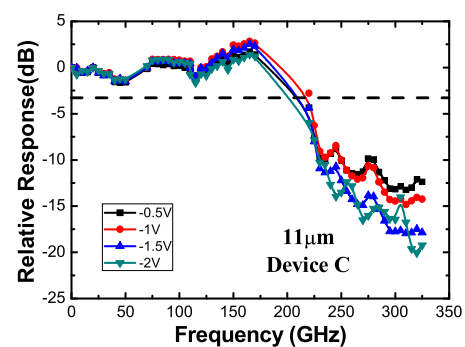


Fig. 8. Bias dependent O-E frequency responses measured under a fixed output photocurrent as 5 mA for device C with an active diameter of 11  $\mu\text{m}$ .

analyzer (ranging from 0.01 to 67 GHz). With a further increase in the measurement frequency (75–325 GHz), there were three major sources of insertion loss in our setup, there was frequency dependent insertion loss from the waveguide probe, from the straight WR-10 waveguide section (0.6 dB at 300 GHz)<sup>3</sup>, which is connected with the power sensor head, and from the waveguide taper (0.3 dB at 300 GHz)<sup>3</sup>. For more details, please refer to our previous work [12]. Fig. 5 shows the total frequency response (from dc to 325 GHz) of the insertion loss in our measurement setup. Although there are two gaps (50–75 GHz and 170–220 GHz) in the frequency range of interest (dc to 325 GHz), this should not have any influence on the accuracy of the measurement, as shown in the following discussion.

All the dynamic measurement results presented here, including the O-E frequency responses and the THz output power, have been carefully de-embedded to remove the insertion loss based on the figure.

Figs. 6 to 8 show the bias dependent O-E frequency responses measured under a fixed output photocurrent at 5 mA for devices A to C, respectively. Here, all the O-E traces can be normalized to the same value of RF power near the DC frequency; the generated RF power of these 3 devices (A to C) is almost the same around the DC. In addition, the optical alignment for the maximum photocurrent remained the same when performing

the bandwidth measurements. Optical misalignment is always accompanied by a fast drop in the photo-generated MMW power, which indicates a significant degradation in the speed of device. This phenomenon can be attributed to the slow lateral drift or diffusion time of the photo-generated carriers in the terrace of the absorption region, where the E-field is much lower than in the center of the active mesa. A similar behavior has been reported for n-side up high-speed avalanche photodiodes (APDs) [22]. The width of the bottom p-type absorber is larger than that of the top n-type collector layer.

Device A exhibits the largest bandwidth of all 3 devices (280 vs. 220 GHz), due to having the smallest active area and parasitic capacitance. Nevertheless, thanks to the undercut profile of the collector layer, the speed performance of devices B and C was much better (220 vs. 75 GHz [14]) than that reported for ultrafast UTC-PDs with similar sized active diameters (of around 10  $\mu\text{m}$ ) and active layer (absorber + collector) thicknesses ( $\sim 300$  nm) [12], [14], [15]. In addition, the optimum bias for high-speed performance of devices A to C happens at  $-1$  V. A further increase in the reverse bias voltage to  $-2$  V would result in degradation of the O-E bandwidth. The fact that this phenomenon is more pronounced in device A can be explained as follows. The root cause of the bandwidth degradation is the electron inter-valley scattering effect under a high applied electric field [10], [23], which leads to an increase in the internal carrier transit time. For device A, the 3-dB bandwidth is closer to the transit time limited bandwidth (280 vs. 542 GHz), which

<sup>3</sup>Virginia Diodes, Inc., 979 Second Street, S.E. Suite 309, Charlottesville, VA 22902-6172. VDI APPLICATION NOTE: Power Measurement above 110 GHz.

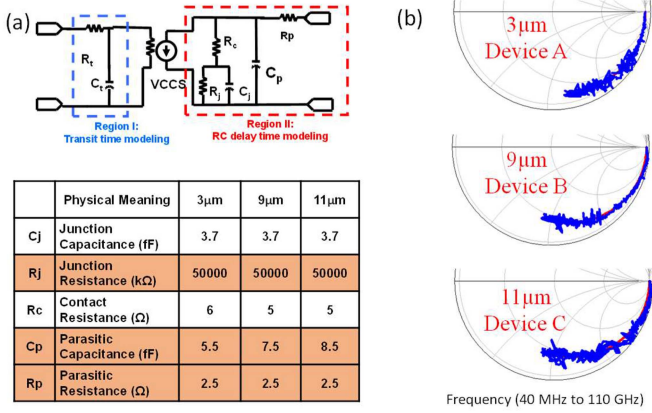


Fig. 9. (a) Equivalent-circuit-model and (b) measured (blue line) and fitted (red lines)  $S_{11}$  parameters from near dc to 110 GHz under a fixed dc bias ( $-1$  V) for devices A to C, without the flip-chip bonding package (bare dies). The table shows the values of the circuit elements used in the modeling process. HFSS: High frequency structural simulator (ANSYS, Inc., Southpointe, 275 Technology Drive, Canonsburg, PA 15317, USA).

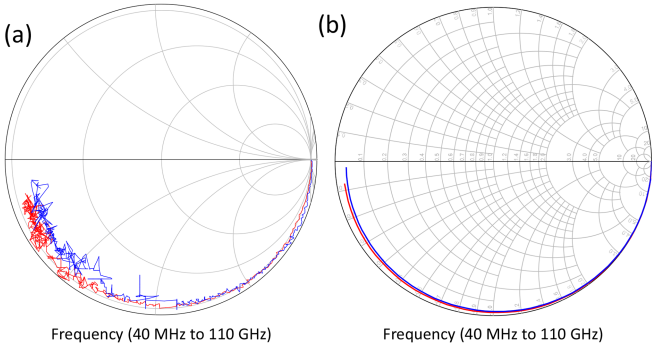


Fig. 10. Smith charts showing the (a) measured and (b) simulated  $S_{11}$  parameters from near dc to 110 GHz for devices A and C with flip-chip bonding packaging under a fixed dc bias ( $-1$  V). Red trace: Device A. Blue trace: Device C.

will be discussed later, than for the other two devices (B and C). This makes the influence of the bias voltages on the net O-E bandwidth the most significant among the three devices. Similar behaviors have been reported in ultrafast UTC-PDs when the 3-dB bandwidth is close to the THz regime ( $\sim 300$  GHz) [10], [12].

The equivalent-circuit modeling technique was used to extract the RC-limited bandwidth for each device structure [18], [19]; see Fig. 9(a). The values used in the fitting process are shown in the inserted table. During the modeling process, the two artificial circuit elements,  $R_T$  and  $C_T$ , are removed in order to extract the extrinsic  $f_{RC}$  of the PD. This is because they are used to mimic the low-pass frequency response of the internal carrier transit time [18], [19]. The measured and simulated frequency responses for the microwave reflection coefficient parameter ( $S_{11}$ ) under a  $-1$  V bias voltage obtained for devices A to C, without flip-chip bonding packaging (bare dies) are shown on the Smith charts in Fig. 10. Clearly, there is a good match between the simulated and measured results from 40 MHz to 110 GHz. The established equivalent circuit model can now be inserted

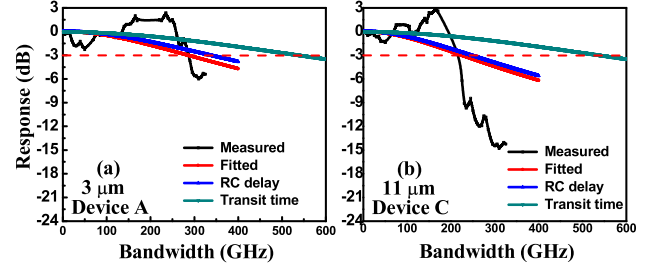


Fig. 11. Measured O-E, extracted RC-limited, transit time, and fitted O-E frequency responses for devices (a) A and (b) C.

into the 3-D structure for the active PD, as shown in Fig. 4(a), for full wave analysis of the whole packaged structure. Fig. 10(a) and (b) show the measured and simulated  $S_{11}$  parameters on a Smith Chart for devices A and C, respectively, after flip-chip bonding packaging. The consistency between the simulation and measurement results indicates the validity of the extracted equivalent circuit models. In addition, as shown in the table inserted in Fig. 9, thanks to the undercut profile in our collector layer, the junction capacitance ( $C_j$ ) is maintained, even with a significant increase in the active diameter from 3 to 11  $\mu\text{m}$ . The degradation in the net O-E bandwidth of devices B and C (see Figs. 6 to 8), can be attributed to the increase in the parasitic capacitance ( $C_p$ ). Although different combinations of  $C_j$  and  $C_p$  may be used to fit the measured  $S_{11}$  traces here, there is only a very minor increase in the length of the  $S_{11}$  traces on the Smith Charts between devices A to C, which clearly indicates that our demonstrated undercut structure can effectively minimize the total capacitance of the UTC-PD. Moreover, based on the value of the extracted total capacitance for device C (12.2 fF), the equivalent active diameter of the non-undercut reference sample will be around 3.5  $\mu\text{m}$ , which is almost the same as that of device A (3  $\mu\text{m}$ ). We would thus expect that the improvements in the saturation current, dc responsivity, and alignment tolerance of this non-undercut reference would not be as good as those of device C.

The overall O-E 3-dB bandwidth ( $f_{3dB}$ ) of our PD is determined from the carrier transport time  $1/f_t$  and the RC time constant  $\frac{1}{f_{RC}}$ . The bandwidth limiting factor of the demonstrated device is calculated using the following equation adapted from [12]:

$$\frac{1}{f_{3dB}^2} = \frac{1}{f_{RC}^2} + \frac{1}{f_t^2} = (2\pi RC)^2 + \frac{1}{f_t^2}, \quad (1)$$

where R is the sum of the parasitic capacitance and the load resistance (50  $\Omega$ ) and C is the total capacitance. Using the established equivalent circuit model, as shown in Fig. 9, we can obtain the RC-limited frequency response. Furthermore, by carefully selecting the values of  $R_T$  and  $C_T$  to fit the measured O-E frequency response, it is possible to determine the internal transit time limited frequency responses. Fig. 11(a) and (b) show the measured O-E, fitted O-E, extracted RC-limited, and transit time limited frequency responses under  $-1$  V for devices A and C, respectively. As can be seen, the extracted transit time limited bandwidth (0.54 THz) is far above the net O-E bandwidth

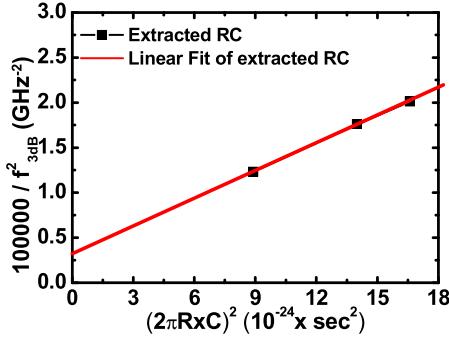


Fig. 12. Extracted  $(1/f_{RC})^2$  versus the measured  $(10^5/f_{3dB}^2)$  for devices A to C.

and  $f_{RC}$  is the major bandwidth limiting factor of both devices. This result suggests that a further improvement in the flip-chip bonding package structure is essential to increase the speed of the proposed ultra-fast PD.

Equation (1) can also be used to calculate the internal carrier transit time. Fig. 12 depicts the values of  $(1/f_{RC})^2$  versus  $(10^5/f_{3dB}^2)$  for the fabricated PDs (A to C). The internal carrier transit times for each device were calculated using (1) and the fitted RC-limited and measured net O-E bandwidths (see Figs. 6 to 8), from the intercepts along the y-axis in Fig. 12 [12]. The obtained  $f_t$  is approximately 0.54 THz, which closely matches the transit time limited bandwidth obtained using the equivalent circuit modeling technique, as seen in Fig. 11.

The extracted averaged electron drift-velocity through the  $\sim 250$  nm depleted  $\text{In}_{0.53}\text{Ga}_{0.47}\text{As}$  and InP collector layer is around  $3.5 \times 10^5$  m/sec. This number suggests that non-equilibrium electron transport plays an important role in the proposed epi-layer structure [10], [22] for THz operation.

Fig. 13(a) to (c) show the measured photo-generated MMW power at an operation frequency of 165 GHz versus the output photocurrent for devices A to C, respectively, obtained under different reverse biases ( $-0.5$  to  $-2$  V) with the two-laser heterodyne-beating setup. The ideal relation between the MMW power and average photocurrent (solid line) with a 100% optical modulation depth under a  $50 \Omega$  load is also plotted for reference. Although all three devices have the same collector width, which implies that they should have the same output photocurrent density and space-charge screening effect [8], we can clearly see that device C has the largest saturation current and output power under a  $-1$  V bias among the 3 devices. This can be attributed to device C having the largest active diameter and the least device heating under high-power operation [24]. For all 3 devices, there is a significant decrease in the maximum output power with a further increase in the reverse bias voltage to  $-2$  V. This phenomenon closely matches the trend shown by the measured bias dependent O-E frequency responses illustrated in Figs. 6 to 8. Overall, the static and dynamic measurement results support the conclusion that the use of an undercut collector profile in the UTC-PD structure can effectively improve the saturation current, dc responsivity, and alignment tolerance, with much less O-E bandwidth degradation, in contrast to directly increasing the

TABLE I  
BENCHMARK VALUES REPORTED FOR ULTRA-FAST PDs

	Device size (d= $\mu\text{m}$ or area= $\mu\text{m}^2$ )	Bandwidth (GHz)	Responsivity (A/W)	Maximum saturation current (mA) @ RF output power @ measure frequency	Saturation current & Bandwidth Product (mA*GHz)
[14]	10 $\mu\text{m}$	75	0.11	25.1mA@1.2dBm@160GHz 25.3mA@-10.5dBm@300GHz	1882 mA*GHz 1897mA*GHz
[16]	2x17 $\mu\text{m}^2$	70	0.25	20mA@-2.5dBm@280GHz	1400mA*GHz
[15]	3 $\mu\text{m}$	230	0.07	5.85mA@-4.94dBm@220GHz	1346mA*GHz
This work	3 $\mu\text{m}$	285	0.1	7mA@-2.4dBm@165GHz 7mA@-2.7dBm@235GHz 7mA@-2.2dBm@235GHz	1995 mA*GHz
This work	11 $\mu\text{m}$	220	0.11	9mA@0.3dBm@165GHz 9mA@-7.3dBm@220GHz	1980 mA*GHz
[12]	3 $\mu\text{m}$	320	0.11	13mA@-3.2dBm@320GHz	4160mA*GHz
Our previous work					

active diameter of the PD. Compared with device C without the undercut profile, as discussed in the section about dc responsivity measurement, there is a minor degradation in the saturation current ( $\sim 10$  vs. 9 mA) of the device with the undercut profile due to its narrower collector width, which impedes thermal dissipation from the absorber to the InP substrate. Nevertheless, in our flip-chip bonding packaged device, some of the generated heat from the absorption layer can be directly dissipated through the Au/Sn pillar and AlN carrier substrate [24]. This renders the difference in the saturation current between the devices with and without undercut profile less apparent.

As can be seen in Figs. 14 and 15, the measured bias dependent MMW power vs. output photocurrent of the 3 devices (A - C) but at higher operating frequencies is close to their 3-dB O-E bandwidths. There is a total difference of around 6.5 dB between the measured and ideal photo-generated THz power, under the same amount of output photocurrent, as specified in these figures. This discrepancy arises mainly from two factors. One is the nearly 3-dB high-frequency roll-off from the PD itself, when operated at near the 3-dB bandwidth (0.285 THz for device A). The other 3 dB loss originates because the optical modulation depth in our two-laser heterodyne-beating system at the near THz frequency separation is only around 65% [12]. We can clearly see that although device A has a smaller saturation current than device B or C (7 vs. 9 mA), it exhibits a higher THz output power ( $-2.7$  vs.  $-7.3$  dBm) at a close operation frequency (235 vs. 220 GHz). This is because device A has the widest 3-dB bandwidth (285 vs. 220 GHz) among the 3 devices. This leads to less high-frequency roll-off when the operating frequency is at around the PD's 3-dB bandwidth.

Table I shows the reported benchmarks for saturation current bandwidth products (SCBPs) of ultra-fast UTC-PDs. Here, the quoted saturation current numbers indicate where the maximum RF power was measured. As can be seen, with the exception of the UTC-PD with a type-II hybrid absorber described in a previous work [12], our demonstrated NBUTC-PD with its undercut collector profile and flip-chip bonding package has the largest SCBP reported, which can be attributed to the good heat-sinking and wide-bandwidth characteristics of our flip-chip bonding package. Although the SCBP values reported in [14], [15], [16] are based on on-wafer measurement, which may also be further improved after the incorporation of more advanced packaging, the comparison in this Table should still be fair, because of the degradation in the bandwidth for the additional flip-chip bonding package process, as discussed in the introduction to this work.

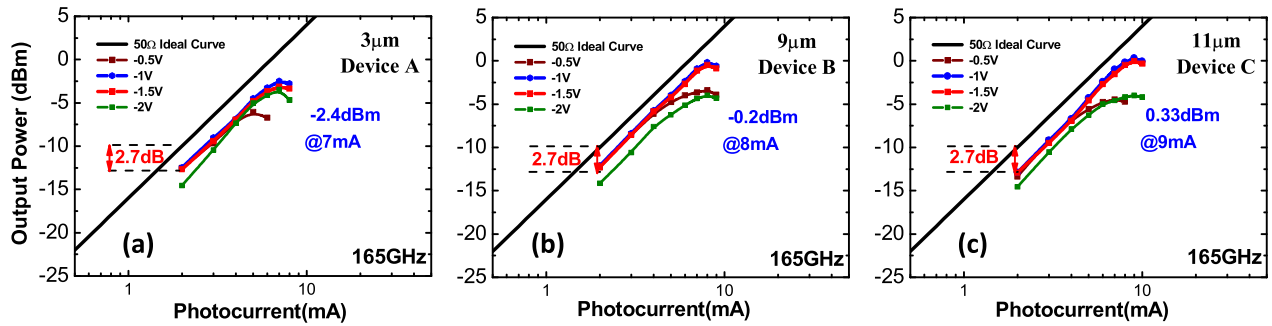


Fig. 13. Measured photo-generated MMW power versus photocurrent for (a) devices A, (b) B, and (c) C with different active diameters under sinusoidal signal excitation and with different reverse biases at the same operating frequency of 165 GHz. The solid line shows the ideal trace for a 100% optical modulation depth and 50  $\Omega$  load.

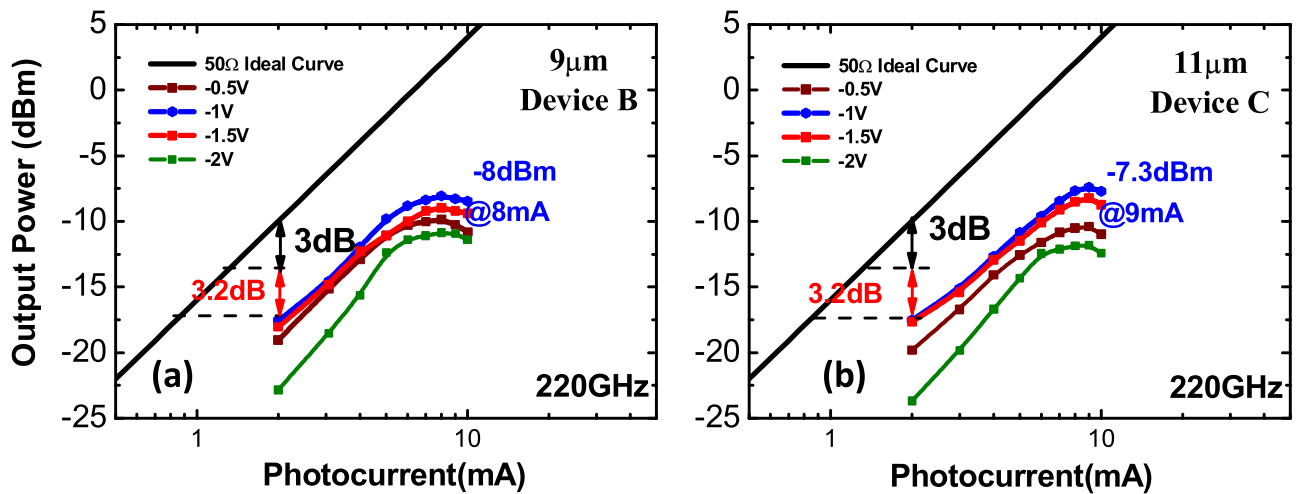


Fig. 14. Measured photo-generated MMW power versus photocurrent for (a) devices B, and (b) C with different active diameters under sinusoidal signal excitation and with different reverse biases at the same operating frequency of 220 GHz. The solid line shows the ideal trace for a 100% optical modulation depth.

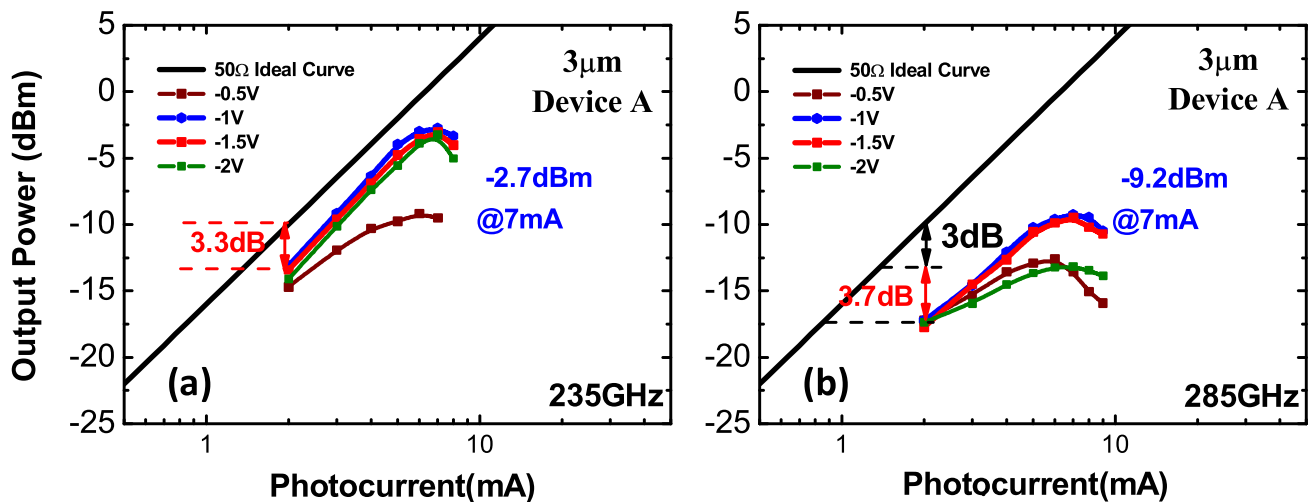


Fig. 15. Measured photo-generated MMW power versus photocurrent for device A at different operating frequency as (a) 235, and (b) 285 GHz under sinusoidal signal excitation and with different reverse biases. The solid line shows the ideal trace for a 100% optical modulation depth.

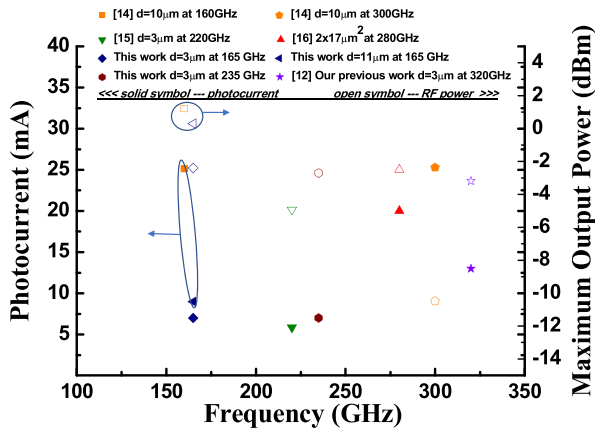


Fig. 16. Saturation output photocurrents and maximum THz output power reported for ultrafast PDs at different operating frequencies. Circles represent the performance of the devices in this work and [14].

Furthermore, as discussed above and illustrated in Figs. 6 to 8, our unique undercut structure allows for an enlargement of the active diameter of the device as well as the saturation current with only a minor degradation in O-E bandwidth. This is also beneficial to the SCBP performance. However, the highest SCBP value was obtained with our previously demonstrated UTC-PD with the type-II hybrid absorber ( $\text{GaAs}_{0.5}\text{Sb}_{0.5}/\text{In}_{0.53}\text{Ga}_{0.47}\text{As}$ ) [12]. The value is higher because the extracted electron drift-velocity is much faster ( $7$  vs.  $3.5 \times 10^5$  m/sec) than that of the UTC-PD with the traditional  $\text{In}_{0.53}\text{Ga}_{0.47}\text{As}$  absorber described in this work. This would lead to a higher saturation current and larger O-E bandwidth. The results suggest that we can further improve the SCBP values of ultrafast UTC-PDs by combining the type-II hybrid absorber with the undercut collector profile demonstrated here. Fig. 16 shows the benchmarks of maximum output THz power and saturation currents reported for ultrafast UTC-PDs at different operation frequencies. We can clearly see that, in comparison to values reported for UTC-PDs with the same active diameter ( $\sim 10 \mu\text{m}$ ) at a similar operating frequency (around 165 GHz), the value of the THz output power is close in value (around +1 dBm) and the DC responsivity (0.11 A/W) the same but with a much lower output photocurrent (25 vs. 9 mA). The more efficient THz power generation of our device can be attributed to its larger 3-dB O-E bandwidth (220 vs. 75 GHz). Such superior speed performance leads to a much lower high-frequency roll-off (+1 vs. -7 dB), as discussed in Figs. 6 to 8, in the O-E frequency response. It in turn results in a much lower required photocurrent (25 vs. 9 mA) and optical power for delivering the close value of MMW power (around +1 dBm) at the same operating frequency ( $\sim 165$  GHz). The demonstrated ultrafast PD structure opens up new paths to further enhance the optical power budget for 6G wireless communication systems with internal optics.

#### IV. CONCLUSION

In conclusion, we demonstrate a novel UTC-PD structure which can fundamentally relax the trade-offs among the saturation current, speed and DC responsivity. Through the use of

an undercut collector profile and an improved flip-chip bonding package we can moderately enlarge the active diameter of an ultra-fast UTC-PD to attain a higher saturation current, larger DC responsivity, and optical alignment tolerance with only a minor degradation in the O-E bandwidth. Compared with the values reported for ultra-fast UTC-PDs with the same sized active diameter of around  $10 \mu\text{m}$ , our device can deliver the same sub-THz output power (around +1 dBm at 165 GHz) with the same DC responsivity but at a much lower output photocurrent (25 vs. 9 mA), because of its faster speed performance. It can thus be expected that our demonstrated device structure can generate THz power in a more efficient way and provide a larger optical power budget for the next generation of RoF wireless communication systems.

#### REFERENCES

- [1] [Online]. Available: <https://precisionmmw.com/what-is-6g/>
- [2] I. A. Alimi, A. L. Teixeira, and P. P. Monteiro, "Toward an efficient C-RAN optical fronthaul for the future networks: A tutorial on technologies, requirements, challenges, and solutions," *IEEE Commun. Surveys Tut.*, vol. 20, no. 1, pp. 708–769, Firstquarter 2018, doi: [10.1109/COMST.2017.2773462](https://doi.org/10.1109/COMST.2017.2773462).
- [3] L. A. Rusch and X. Guan, "Silicon photonics for high-speed 5G and optical networks," in *Proc. Opt. Fiber Commun. Conf. Exhib.*, 2023, pp. 1–3, doi: [10.1364/OFC.2023.Tu2B.2](https://doi.org/10.1364/OFC.2023.Tu2B.2).
- [4] A. Stöhr et al., "Millimeter-wave photonic components for broadband wireless systems," *IEEE Trans. Microw. Theory Tech.*, vol. 58, no. 11, pp. 3071–3082, Nov. 2010.
- [5] S. Koenig et al., "Wireless sub-THz communication system with high data rate," *Nature Photon.*, vol. 7, pp. 977–981, Dec. 2013.
- [6] J.-W. Shi, C.-B. Huang, and C.-L. Pan, "Millimeter-wave photonic wireless links for very-high data rate communication," *NPG Asia Mater.*, vol. 3, no. 2, pp. 41–48, Apr. 2011.
- [7] H.-J. Song and T. Nagatsuma, "Present and future terahertz communications," *IEEE Trans. Terahertz Sci. Tech.*, vol. 1, no. 1, pp. 256–263, Sep. 2011.
- [8] K. Kato, "Ultrawide-band/high-frequency photodetectors," *IEEE Trans. Microw. Theory Tech.*, vol. 47, no. 7, pp. 1265–1281, Jul. 1999.
- [9] H. Ito, S. Kodama, Y. Muramoto, T. Furuta, T. Nagatsuma, and T. Ishibashi, "High-speed and high-output InP-InGaAs untraveling-carrier photodiodes," *IEEE J. Sel. Topics Quantum Electron.*, vol. 10, no. 4, pp. 709–727, Jul./Aug. 2004.
- [10] T. Ishibashi, Y. Muramoto, T. Yoshimatsu, and H. Ito, "Untraveling-carrier photodiodes for terahertz applications," *IEEE J. Sel. Topics Quantum Electron.*, vol. 20, no. 6, Nov./Dec. 2014, Art. no. 3804210.
- [11] J.-W. Shi, F.-M. Kuo, and J. E. Bowers, "Design and analysis of ultra-high speed near-ballistic uni-traveling-carrier photodiodes under a  $50 \Omega$  load for high-power performance," *IEEE Photon. Technol. Lett.*, vol. 24, no. 7, pp. 533–535, Apr. 2012.
- [12] J.-M. Wun, Y.-W. Wang, and J.-W. Shi, "Ultra-fast uni-traveling carrier photodiodes with  $\text{GaAs}_{0.5}\text{Sb}_{0.5}/\text{In}_{0.53}\text{Ga}_{0.47}\text{As}$  type-II hybrid absorbers for high-power operation at THz frequencies," *IEEE J. Sel. Topics Quantum Electron.*, vol. 24, no. 2, Mar./Apr. 2018, Art. no. 8500207.
- [13] Z. Li, H. Pan, H. Chen, A. Beling, and J. C. Campbell, "High-saturation current modified uni-traveling-carrier photodiode with cliff layer," *IEEE J. Quantum Electron.*, vol. 46, no. 5, pp. 626–632, May 2010.
- [14] J. S. Morgan et al., "Bias-insensitive  $\text{GaAsSb}/\text{InP}$  CC-MUTC photodiodes for mmWave generation up to 325 GHz," *J. Lightw. Technol.*, vol. 41, no. 23, pp. 7092–7097, Dec. 2023, doi: [10.1109/JLT.2023.3298772](https://doi.org/10.1109/JLT.2023.3298772).
- [15] Y. Tian et al., "Ultrafast MUTC photodiodes over 200 GHz with high saturation power," *Opt. Exp.*, vol. 31, no. 15, pp. 23790–23800, Jul. 2023.
- [16] M. Grzeslo et al., "High saturation photocurrent THz waveguide-type MUTC-photodiodes reaching mW output power within the WR3.4 band," *Opt. Exp.*, vol. 31, pp. 6484–6498, Feb. 2023.
- [17] [Online]. Available: [https://www.albisopto.com/albis\\_product/pd50x1-on-carrier-112-gbaud-photodiode-with-integrated-lens/](https://www.albisopto.com/albis_product/pd50x1-on-carrier-112-gbaud-photodiode-with-integrated-lens/)

- [18] J.-M. Wun, C.-H. Lai, N.-W. Chen, J. E. Bowers, and J.-W. Shi, "Flip-chip bonding packaged THz photodiode with broadband high-power performance," *IEEE Photon. Technol. Lett.*, vol. 26, no. 24, pp. 2462–2464, Dec. 2014.
- [19] Nan-Wei Chen Naseem et al., "Simultaneous enhancement of the bandwidth and responsivity in high-speed avalanche photodiodes with an optimized flip-chip bonding package," *Opt. Exp.*, vol. 31, pp. 26463–26473, 2023.
- [20] I.-H. Tan et al., "120-GHz long-wavelength low-capacitance photodetector with an air-bridged coplanar metal waveguide," *IEEE Photon. Technol. Lett.*, vol. 7, no. 12, pp. 1477–1479, Dec. 1995, doi: [10.1109/68.477288](https://doi.org/10.1109/68.477288).
- [21] J.-W. Shi, C.-Y. Wu, Y.-S. Wu, P.-H. Chiu, and C.-C. Hong, "High-speed, high-responsivity, and high-power performance of near-ballistic uni-traveling-carrier photodiode at 1.55  $\mu\text{m}$  wavelength," *IEEE Photon. Technol. Lett.*, vol. 17, no. 9, pp. 1929–1931, Sep. 2005.
- [22] M. Nada, Y. Muramoto, H. Yokoyama, T. Ishibashi, and H. Matsuzaki, "Triple-mesa avalanche photodiode with inverted P-down structure for reliability and stability," *J. Lightw. Technol.*, vol. 32, no. 8, pp. 1543–1548, Apr. 2014.
- [23] T. Ishibashi, "Nonequilibrium electron transport in HBTs," *IEEE Trans. Electron Devices*, vol. 48, no. 11, pp. 2595–2604, Nov. 2001.
- [24] A. Beling, X. Xie, and J. C. Campbell, "High-power, high-linearity photodiodes," *Optica*, vol. 3, pp. 328–338, Mar. 2016.

**Yu-Cyuan Huang** was born in Taipei, Taiwan, on July 10, 1999. He received the M.S. degree from the Department of Electrical Engineering, National Central University, Taoyuan, Taiwan, in 2023. His research interests include uni-traveling photodiodes and avalanche photodiodes.

**Nan-Wei Chen** received the B.S. degree in atmospheric science and the M.S. degree in space science from National Central University, Jhongli, Taiwan, in 1993 and 1995, respectively, and the Ph.D. degree in electrical engineering from the University of Illinois at Urbana-Champaign (UIUC), Champaign, IL, USA, in 2004. He is currently a Full Professor with the Department of Electrical Engineering as well as the Director of the International Bachelor Program in Electrical and Communication Engineering, Yuan Ze University, Taoyuan, Taiwan. From 1998 to 2004, he was a Research Assistant with the Center for Computational Electromagnetics, University of Illinois. In 2004, he joined the Department of Electrical Engineering, National Central University, Taiwan, as an Assistant Professor. In February 2010, he joined the Department of Communications Engineering, Yuan Ze University, as an Associate Professor. His research interests include microwave/millimeter wave circuit and antenna designs, computational electromagnetics, and periodic structures. Dr. Chen was the recipient of the Raj Mittra Outstanding Research Award at UIUC in 2004. He was the Vice Chairman of the IEEE Antennas and Propagation Society Taipei chapter from 2018 to 2019.

**Yen-Kun Wu** was born in Taichung, Taiwan, on October 26, 1997. He is currently working toward the Master's degree with the Department of Electrical Engineering, National Central University, Taoyuan, Taiwan. His research interests include uni-traveling photodiodes and avalanche photodiodes.

**Naseem** was born in the Punjab, India, in 1991. He received the M.Tech. degree from the Department of Nanotechnology, Jamia Millia Islamia, New Delhi, India, and the Ph.D. degree from the Department of Electrical Engineering, National Central University, Taiwan, in May 2023. His research interests include high-speed photodiodes and avalanche photodiodes for optical receivers.

**Jin-Wei Shi** (Senior Member, IEEE) was born in Kaohsiung, Taiwan, on January 22, 1976. He received the B.S. degree in electrical engineering from National Taiwan University, Taipei, Taiwan, in 1998, and the Ph.D. degree from the Graduate Institute of Electro-Optical Engineering, National Taiwan University in 2002. He was a Visiting Scholar with the University of California, Santa Barbara (UCSB), Santa Barbara, CA, USA, in 2000 and 2001. From 2002 to 2003, he was a Postdoc with the Electronic Research and Service Organization (ERSO) of the Industrial Technology Research Institute. In 2003, he joined the Department of Electrical Engineering, National Central University, Taoyuan, Taiwan, where he is currently a Professor. In 2011, he again joined the ECE Department of UCSB as a Visiting Scholar. He has authored or coauthored more than 170 Journal papers, 160 conference papers and hold 20 patents. His research interests include ultra-high speed/power optoelectronic devices, such as photodetectors, electro-absorption modulators, sub-millimeter wave photonic transmitters, and semiconductor lasers. He was an invited speaker at the 2002 IEEE LEOS, 2005 SPIE Optics East, 2007 Asia-Pacific Microwave Photonic conference (AP-MWP), 2008 Asia Optical Fiber Communication & Optoelectronic Exposition & Conference (AOE), 2011 Optical Fiber Communication (OFC), and 2012 IEEE Photonic Conference (IPC). He was the technical program committees for the OFC 2009-2011, 2012 SSDM, 2012 MWP, and 2013 Asia-Pacific CLEO. In 2007, he was the recipient of the Excellent Young Researcher Award from the Association of Chinese IEEE and in 2010 he was the recipient of the Da-You Wu Memorial Award. He has been an Optica fellow since 2023 and senior member of IEEE since 2012. He was also an Associate Editor for *Optics Express* in 2017.